JOM, Vol. 69, No. 8, 2017
DOI: 10.1007/s11837-017-2397-4

Columnar and Equiaxed Solidification of Al-7 wt.% Si Alloys in Reduced Gravity in the Framework of the CETSOL Project

G. ZIMMERMANN,[1,19] L. STURZ,[1] H. NGUYEN-THI,[2] N. MANGELINCK-NOEL,[2] Y.Z. LI,[2] C.-A. GANDIN,[3] R. FLEURISSON,[3] G. GUILLEMOT,[3] S. MCFADDEN,[4,5] R.P. MOONEY,[4] P. VOORHEES,[6] A. ROOSZ,[7] A. RONAFÖLDI,[7] C. BECKERMANN,[8] A. KARMA,[9] C.-H. CHEN,[9] N. WARNKEN,[10] A. SAAD,[11] G.-U. GRÜN,[12] M. GROHN,[13] I. POITRAULT,[14] T. PEHL,[15] I. NAGY,[16] D. TODT,[17] O. MINSTER,[18] and W. SILLEKENS[18]

1.—ACCESS e.V., 52072 Aachen, Germany. 2.—Universite Aix Marseille, CNRS, IM2NP, 13397 Marseille, France. 3.—MINES Paris Tech CEMEF, 06904 Sophia Antipolis, France. 4.—Department of Mechanical and Manufacturing Engineering, Trinity College Dublin, Dublin 2, Ireland, UK. 5.—Ulster University, Magee Campus, Londonderry BT48 7JL, Northern Ireland, UK. 6.—Northwestern University, Evanston, IL 60208, USA. 7.—Department of Physical Metallurgy, University of Miskolc, Miskolc-Egyetemvaros 3515, Hungary. 8.—University of Iowa, Iowa City, IA 52242, USA. 9.—Physics Department, Northeastern University, Boston, MA 02115, USA. 10.—School of Metallurgy and Materials, University of Birmingham, Birmingham B15 2TT, UK. 11.—TRANSVALOR, 06255 Mougins Cedex, France. 12.—HYDRO Aluminium Rolled Products GmbH, 53117 Bonn, Germany. 13.—Incaal GmbH, 52388 Nörvenich, Germany. 14.—ArcelorMittal Industeel, 71201 Le Creusot Cedex, France. 15.—Arconic-Köfém Ltd., Székesfehérvár 8000, Hungary. 16.—INOTAL Aluminiumfeldolgozo, Varpalota 8104, Hungary. 17.—NEMAK Györ Kft., Gyor 9027, Hungary. 18.—ESTEC, 2201 AZ Noordwijk, The Netherlands. 19.—e-mail: g.zimmermann@access-technology.de

During casting, often a dendritic microstructure is formed, resulting in a columnar or an equiaxed grain structure, or leading to a transition from columnar to equiaxed growth (CET). The detailed knowledge of the critical parameters for the CET is important because the microstructure affects materials properties. To provide unique data for testing of fundamental theories of grain and microstructure formation, solidification experiments in microgravity environment were performed within the European Space Agency Microgravity Application Promotion (ESA MAP) project Columnar-to-Equiaxed Transition in SOLidification Processing (CETSOL). Reduced gravity allows for purely diffusive solidification conditions, i.e., suppressing melt flow and sedimentation and floatation effects. On-board the International Space Station, Al-7 wt.% Si alloys with and without grain refiners were solidified in different temperature gradients and with different cooling conditions. Detailed analysis of the microstructure and the grain structure showed purely columnar growth for nonrefined alloys. The CET was detected only for refined alloys, either as a sharp CET in the case of a sudden increase in the solidification velocity or as a progressive CET in the case of a continuous decrease of the temperature gradient. The present experimental data were used for numerical modeling of the CET with three different approaches: (1) a front tracking model using an equiaxed growth model, (2) a three-dimensional (3D) cellular automaton–finite element model, and (3) a 3D dendrite needle network method. Each model allows for predicting the columnar dendrite tip undercooling and the growth rate with respect to time. Furthermore, the positions of CET and the spatial extent of the CET, being sharp or progressive, are in reasonably good quantitative agreement with experimental measurements.

(Published online June 1, 2017)

INTRODUCTION

Materials properties of cast components are determined strongly by their microstructures. During casting, often a dendritic microstructure is formed. As a result of competition among the growth of several arrays of dendrites, columnar or equiaxed grain structures are formed, or a transition from columnar to equiaxed growth is observed. The precise investigation on grain formation is hampered by buoyancy–driven flow and by movement of crystals growing in the melt. To allow for pure diffusive solidification conditions, i.e., suppressing melt flow and sedimentation effects, experiments in microgravity environment were performed. These experiments provide unique data for testing fundamental theories of grain and microstructure formation.

Such activities are the task of the research project Columnar-to-Equiaxed Transition in SOLidification Processing (CETSOL) in the framework of the Microgravity Application Promotion (MAP) programme of the European Space Agency (ESA). At present, the CETSOL team consists of seven European scientific partners, three partners from the United States and seven partners from industry (see list of co-authors).

MICROGRAVITY EXPERIMENTS WITH Al-7 wt.% Si ALLOYS

Experimental Setup and Process Parameters

Several experiments in microgravity were carried out successfully to investigate the columnar-to-equiaxed transition under diffusive conditions for heat and mass transport.

First, within Batch1 (B1), six solidification experiments were performed in the Materials Science Laboratory (MSL) with the Low Gradient Furnace (LGF) module on-board the International Space Station (ISS). Rod-like samples with a diameter of 7.8 mm and a length of 245 mm made of Al-7 wt.% Si alloy, with (gr) and without grain refiner particles, were used and integrated in a special sample cartridge assembly (SCA) together with 12 thermocouples positioned along the sample (Fig. 1). The main parts of the LGF are the "cold zone," which consists of three heaters; the "hot zone," which consists of four heaters; and an adiabatic zone in between. By controlling the temperatures of the heaters, a temperature gradient develops along the sample axis. Melting or solidification of the metallic alloy is realized by movement of the furnace insert along the axis of the fixed sample with a defined speed. Table I summarizes the main parameters of the Batch1 flight experiments. At the beginning of the solidification phase, the furnace is in its end position and the set heater temperatures allow for an initial temperature gradient along the sample axis of about 0.9 K/mm. The solidification stage I with $v_1 = 10$ μm/s for $z_1 = 20$ mm was identical for all experiments (see Table I) and is expected to generate a columnar dendritic growth. A transition to equiaxed growth should be triggered in the solidification stage II, either by increasing the furnace movement to $v_2 = 200$ μm/s (B1-FM1 to B1-FM3) or mainly by decreasing the temperature gradient by applying a cooling rate of $dT/dt = -4$ K/min at the heaters of the hot zone (B1-FM4 to B1-FM6).

Second, within Batch2a (B2), seven solidification experiments were performed in the MSL with the Solidification and Quenching Furnace (SQF) module on-board the ISS. As with Batch1, rod-like samples of Al-7 wt.% Si alloys with the same dimensions made, with (gr) and without grain refiner particles, were used and integrated in a sample cartridge assembly (SCA) together with 12 thermocouples positioned along the sample. The positions of the 12 thermocouples TC1 to TC12 are regularly distributed from −7.5 mm to 222.5 mm from the cold end of the sample. The SQF consists of a hot zone (four heaters), an actively cooled cold zone realized by a liquid metal ring (LMR), and an adiabatic zone in between. By controlling the temperatures of the heater, a higher temperature gradient along the sample axis (than in Batch1) was achieved. Melting or solidification of the metallic alloy was realized by movement of the furnace insert along the axis of the fixed sample with a defined speed. Table II summarizes the main parameters of the Batch2a flight experiments. At the beginning of the solidification phase, the furnace is in its end position and the heater set temperatures allow for an initial temperature gradient along the sample axis of about 4 K/mm and 3 K/mm (B2-FM4 and B2-FM7). The solidification stage I with $v_1 = 20$ μm/s for $z_1 = 20$ mm or $z_1 = 30$ mm is expected to generate columnar dendritic growth. A transition to equiaxed growth should be triggered in the solidification stage II, either by increasing the furnace movement to $v_2 = 200$ μm/s (B2-FM1 to B2-FM4) or by decreasing the temperature gradient by applying a cooling rate of $dT/dt = -8$ K/min at the heaters of the hot zone (B2-FM5 to B2-FM7). For the nonrefined samples FM2 and FM6, a moderate rotating magnetic field (RMF) with frequency $f = 57$ Hz and magnetic flux density $B = 0.5$ mT was applied to promote eventual fragmentation.

Experimental Results

Based on the temperature measurements along the sample axis, the cooling curves for all Batch1 and Batch2a samples were determined. Also, the average liquidus isotherm velocities and the temperature gradients ahead of the liquidus isotherm were deduced as a function of time. It was found that grain refinement and RMF have almost negligible influence on the heat flow.

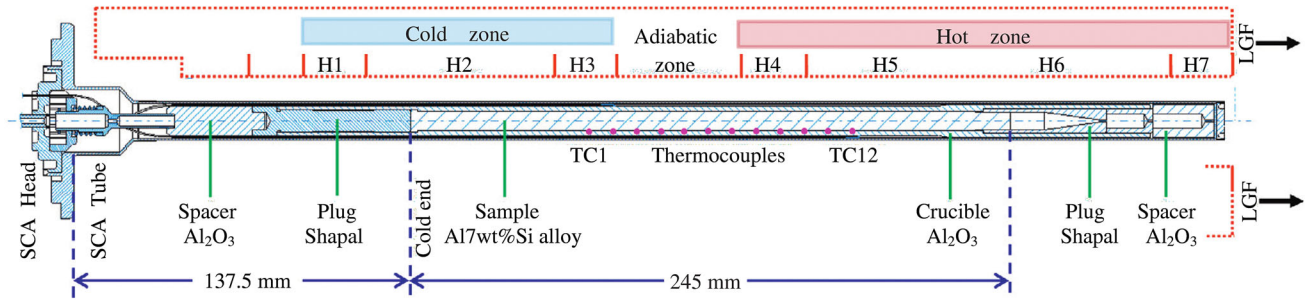

Fig. 1. Schematic setup of the sample cartridge assembly (SCA) inserted in the low gradient furnace (LGF) available in the Materials Science Laboratory (MSL) on board the International Space Station (ISS). The SCA contains the Al–7 wt.% Si alloy inserted as a 7.8-mm-diameter, 245-mm-long cylinder. The LGF is sketched at its initial position with respect to the SCA. The positions of the 12 thermocouples TC1 to TC12 regularly distributed from 72.5 mm to 182.5 mm from the cold end of the sample are also provided.

Table I. Process parameters of the CETSOL1 MSL-LGF Batch1 (B1) flight experiments

CETSOL Batch1 Sample no.	Alloy	Homogenization time t_H (min)	Solidification Stage I		Solidification Stage II			Fast movement Stage III
			v_1 (μm/s)	z_1 (mm)	v_2 (μm/s)	z_2 (mm)	dT/dt (K/min)	v_3 (μm/s)
B1-FM1	AlSi7 + gr	10	10	20	200	50	–4	3000
B1-FM2	AlSi7 + gr	300	10	20	200	50	–4	3000
B1-FM3	AlSi7	300	10	20	200	50	–4	3000
B1-FM4	AlSi7	300	10	20	10	20	–4	3000
B1-FM5	AlSi7 + gr	10	10	20	10	20	–4	3000
B1-FM6	AlSi7 + gr	300	10	20	10	20	–4	3000

Table II. Process parameters of the CETSOL MSL-LGF Batch2a (B2) flight experiments

CETSOL Batch2a Sample no.	Alloy	Homogenization time t_H (min)	Solidification Stage I		Solidification Stage II				Quench Stage III
			v_1 (μm/s)	z_1 (mm)	v_2 (μm/s)	z_2 (mm)	dT/dt (K/min)	RMF	
B2-FM1	AlSi7 + gr	240	20	20	200	50	–8	No	Yes
B2-FM2	AlSi7	240	20	20	200	50	–8	Yes	Yes
B2-FM3	AlSi7 + gr	60	20	30	200	50	–8	No	Yes
B2-FM4	AlSi7 + gr	60	20	30	200	50	–8	No	Yes
B2-FM5	AlSi7 + gr	60	20	30	20	50	–8	No	Yes
B2-FM6	AlSi7	60	20	30	20	50	–8	Yes	Yes
B2-FM7	AlSi7 + gr	60	20	30	20	50	–8	No	Yes

From axial and longitudinal cross sections of the samples, the microstructure and grain structures were identified. Quantitative evaluation of the microstructure showed the development of eutectic percentage along the sample axis. From electrolytically etched cross sections observed in a polarizing microscope, the different grain structures were identified. Additionally, from quantitative EBSD measurements, the size (equivalent diameter), the crystallographic orientation, and the elongation factor of each grain was determined. The elongation factor was defined by the ratio of the length of the major axis to the length of the minor axis, the two axes intersecting orthogonally at the centroid of the grain.

Some results for the Batch1 benchmark experiments are already published[1–4] and are summarized here briefly:

- In nonrefined alloys (samples B1-FM3 and B1-FM4; see Table I), no CET was observed, but columnar dendritic growth with some fragmen-

tation of dendrite structures did occur. The fragments have a size comparable with the dendrite side-branch spacing and cannot promote CET during solidification in microgravity environment because the fragments are not transferred by melt convection to the undercooled melt ahead of the columnar front.[3]

- CET was obtained only for refined alloys (see Table I). In the case of the sudden increase of the solidification velocity (samples B1-FM1 and B1-FM2), a sharp CET within a few millimeter distance was observed, based on the evaluation of the grain size. In the case of a decrease of the temperature gradient, resulting also in a moderate increase of solidification velocity, the formation of elongated and equiaxed grains is found (samples B1-FM5 and B1-FM6). At the end of this transition region of several tenths of millimeters, fully equiaxed grains are detected. Therefore, a progressive CET mode exists.

The evaluation of the Batch2a samples is still in progress. As a recent result, in the following section, a comparative analysis of two flight samples—one from Batch1 (B1-FM1) and one from Batch2a (B2-FM1)—is given. Figure 2 shows the microstructure and the eutectic percentage map of the longitudinal central sections situated in the sample at the junction between stage I and II for samples B1-FM1 and B2-FM2. The successive solidification stages (I, II, and III) are marked out on the left side, which were defined by the position of the liquidus isotherm calculated as in our previous work.[3]

For both samples, a columnar structure is obtained during stage I. Some large eutectic regions (darker areas in Fig. 2) are found in stage I, which are formed as a result of the solute rejection during solidification and accumulation in the interdendritic regions. The microstructure significantly changes from stage I to stage II in both samples. First, equiaxed and finer (compared with stage I) dendrite grains are obtained in stage II. Moreover, no large eutectic zones are observed anymore. As a consequence, the eutectic distribution is much more uniform, and the eutectic percentage is also lower in stage II, but nearly the same for B1-FM1 and B2-FM1.[5] In comparison of the two samples, finer structures are obtained in B2-FM1, in every stage, than what can be observed in B1-FM1.

For both samples, the increase of furnace velocity results in a sharp increase of the liquidus isotherm velocity. At lower growth velocity in stage I, competition with neighboring dendrites forms large solute-enriched liquid pockets in the interdendritic region that are later transformed into eutectic phase. But in stage II, the velocity increase leads to a larger undercooling at the front of the solidification. In this case, the Si content is higher according to the phase diagram and the growth rate of the dendrite would be lower. As a result, a more homogeneous eutectic distribution and fine dendritic microstructure are generated. Moreover, when comparing the two samples, we can see that for the same growth velocity, a higher temperature gradient leads to a shorter mushy zone during solidification, which accordingly decreases the growth and ripening time of the dendritic microstructure in this region. Therefore, for other parameters comparable, the increase of the temperature gradient leads to a finer microstructure.

Considering the grain structure observed by optical microscopy, both samples are columnar during stage I and equiaxed in stage II, which confirms a columnar-to-equiaxed transition in both experiments, triggered by the increase of the solidification velocity. Nevertheless, the equiaxed grains in B2-FM1 appear to be more elongated than in B1-FM1. The longest length of the columnar zone is defined as the CET inception,[6] and it is noted CET_{min} in Fig. 2. This position is 127 mm for B1-FM1 and 134 mm for B2-FM1.

For quantitative evaluation of the CET, the grain structure is also investigated using EBSD measurements. Figure 3 shows the grain equivalent diameter and elongation factor longitudinal profiles calculated from the EBSD maps. For both samples, the equivalent diameter decreases from stage I to stage II as expected with an increase of growth rate. According to Hunt's model,[7] a critical value of the elongation factor of the grains was deduced to define the occurrence of CET. Grains would be recognized as fully equiaxed below this value. Here, the value "2" is discussed. In the case of B1-FM1, the elongation factor remains constant and lower than 2 except at one isolated position after CET_{min}, indicating an equiaxed zone covering the stage II and a sharp CET. Similar to B1-FM1, the equivalent diameter of B2-FM1 decreases from stage I to stage II, whereas the elongation factor mainly stays close above 2 after CET_{min} up to 156 mm. Therefore, the equiaxed grains are more elongated in this region defining a progressive CET. It should be noted that an important deviation of the elongation factor is observed for this sample at about 148 mm, which has to be correlated with the existence of the porosity observed in Fig. 2.

A higher velocity enhances the constitutional undercooling ahead of the solidification front, leading to the CET in both samples. Yet, as a result of the higher temperature gradient of 4 K/mm in B2-FM1, nucleation takes place in a shorter undercooled region. Therefore, the nucleation rate is reduced compared with the experiment with temperature gradient of 0.9 K/mm. As a consequence, a

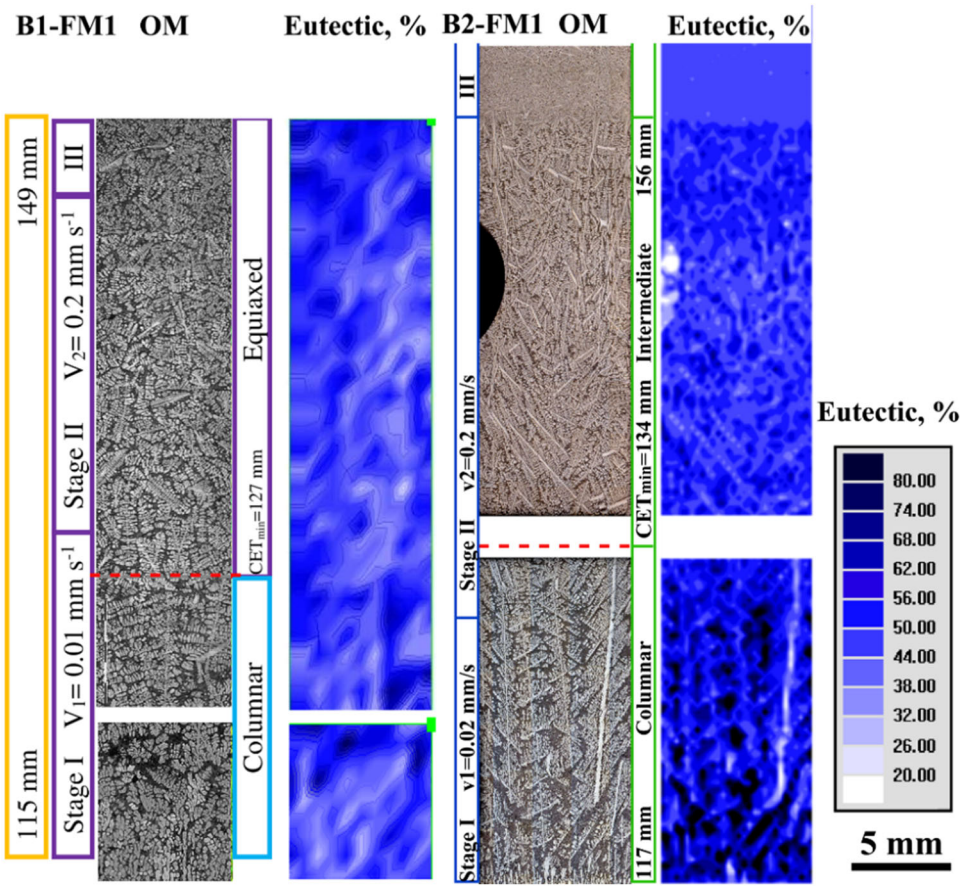

Fig. 2. Longitudinal microstructures determined by optical microscopy (OM) (left) and eutectic percentage distribution maps (right) for flight samples B1-FM1 and B2-FM1. The blank region represents the material loss during sample preparation.

mixed zone of some still columnar growing dendrites and new equiaxed dendrites exist, which can be characterized as a progressive CET in B2-FM1, whereas in B1-FM1, a sharp CET is observed.[5]

NUMERICAL MODELING OF CET

The flight experiments provide unique data for columnar-to-equiaxed transition in Al-7 wt.% Si alloy for pure diffusive solidification conditions, i.e., without melt flow and sedimentation and floatation effects. For this reason, they are used to improve several approaches for numerical modeling of CET, as follows:

- Columnar front tracking model with an equiaxed growth model
- Cellular automaton–finite element (CAFE) method
- Dendritic needle network (DNN) method

CET Modeling Using Front Tracking Approach

An approach that combines front tracking (FT) of columnar growth[8] and an equiaxed volume averaging method[9] was employed to model CET. This model allows for tracking explicitly the undercooled columnar front and for modeling equiaxed nucleation from grain refiners. The results of numerical modeling for some CETSOL Batch1 experiments are published.[1,4,10] For sample B1-FM2 with grain refiner, the simulated prediction of the CET position is in very close agreement with that measured experimentally. Also, for B1-FM2 and B1-FM3 samples, the progress of the columnar front was modeled. It was found that the thermal gradient and formation of undercooled zone ahead of the columnar front were similar for both experiments. Therefore, the effect of grain refiners was crucial for the CET in B1-FM2.

Meanwhile, the 1D Bridgman furnace front tracking model (BFFTM)[11,12] has been significantly modified to simulate columnar and equiaxed growth in the Batch1 flight experiments. The model is suitable for low Biot number (Bi $<$ 0.1) applications. We estimate the maximum Biot number for the experiment to be 0.065. Axial and radial heat flow in the crucible has been incorporated using a 2D axisymmetric model. Also, an equiaxed growth model based on the well-established JMAK model[13–15] has been developed and implemented. The equiaxed growth model is currently being redeveloped to improve

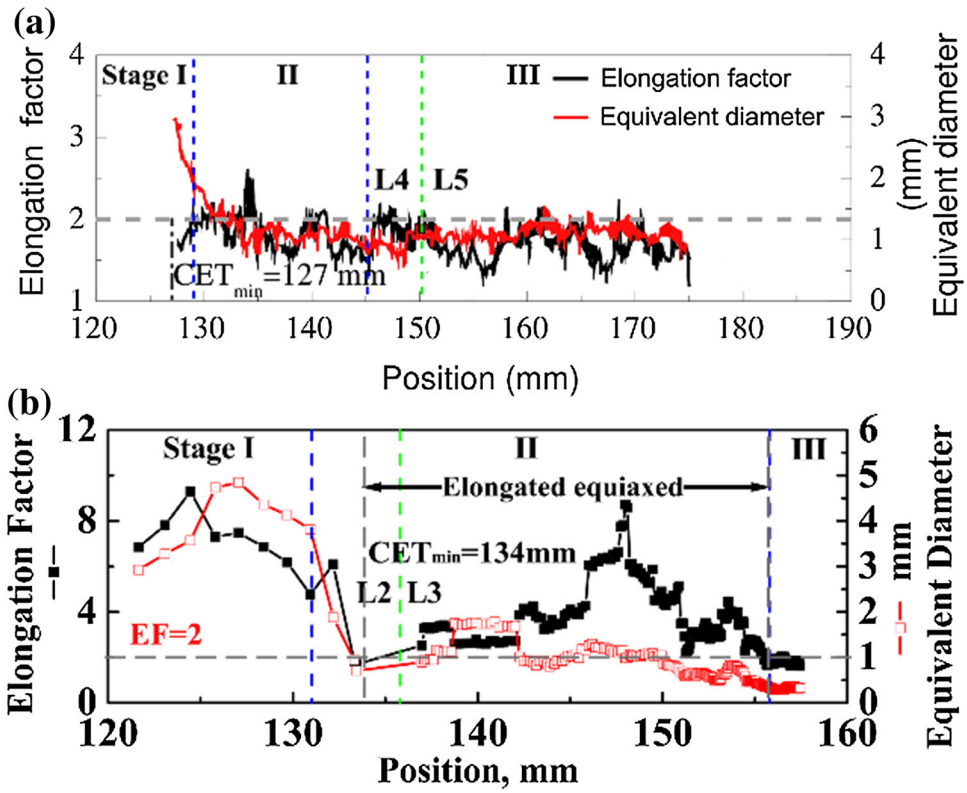

Fig. 3. Longitudinal profiles of the averaged elongation factor and equivalent diameter of the experimental grain contours from EBSD patterns for (a) B1-FM1 and (b) B2-FM1.

computational efficiency. The overriding objective of the thermal modeling carried out has been to provide enlightenment regarding experiment design, conditions pertinent to CET, and cross validation in respect of previous modeling efforts.

Figure 4 illustrates the hybrid of the 2D (annular-shaped control volumes, in black, containing the crucible, Δr = 0.7125 mm) and the 1D (disc-shaped control volumes, in blue, containing the sample, Δx = 0.5 mm) axisymmetric model domains. The models are independent but share (1) a common boundary, (2) grid resolution in the axial direction, and (3) their numerical time step, Δt = 0.001 s.

The equiaxed growth model applies Johnson–Mehl–Avrami–Kolmogorov (JMAK) theory to independently simulate growth of spherical envelopes of equiaxed mush ahead of a columnar front. The thermal history from 12 thermocouples, located inside grooves on the crucible, is used to drive dynamic boundary conditions in the numerical model. Other key inputs to the model are nuclei density (N_o = 1.6 × 10^{10} m^{-3}), and mean (4°C) and standard deviation (0.5°C) of nucleation undercooling (see also Ref. 20). It is worth noting that these nucleation parameters are central to the behavior of the model. Although a typical maximal value for nucleation undercooling can be determined by examining the magnitude of undercooling ahead of the columnar front (in numerical simulations), the standard deviation of a distribution of nucleation events and the maximum nucleation density are more difficult to estimate. These parameters are selected so that the resulting CET matches that observed in the experiment samples. The current model is computationally inefficient at large nuclei densities (>2 × 10^{10} nuclei/m^3); nonetheless, a new algorithm is currently in development that solves this problem.

Figure 5 illustrates the mechanism for equiaxed growth ahead of a progressing columnar front within the BFFTM domain. Useful outputs from the model include a columnar dendrite tip undercooling, growth rate, temperature gradient with respect to time, and sharp or mixed CET prediction capabilities. Good agreement (within 1 mm) is found between the simulated and the experimentally measured CET position in B1-FM2.

CET Modeling Using CAFE Method

The CAFE method was proposed to model complex phenomena occurring during solidification processes through the integration of microscopic laws. Resolutions developed at microscopic and macroscopic scales are modeled.[16–19] The conservation equations for energy, solute mass, and momentum are solved on a tetragonal FE mesh, which is defined on the domain of interest. A grid of cubic

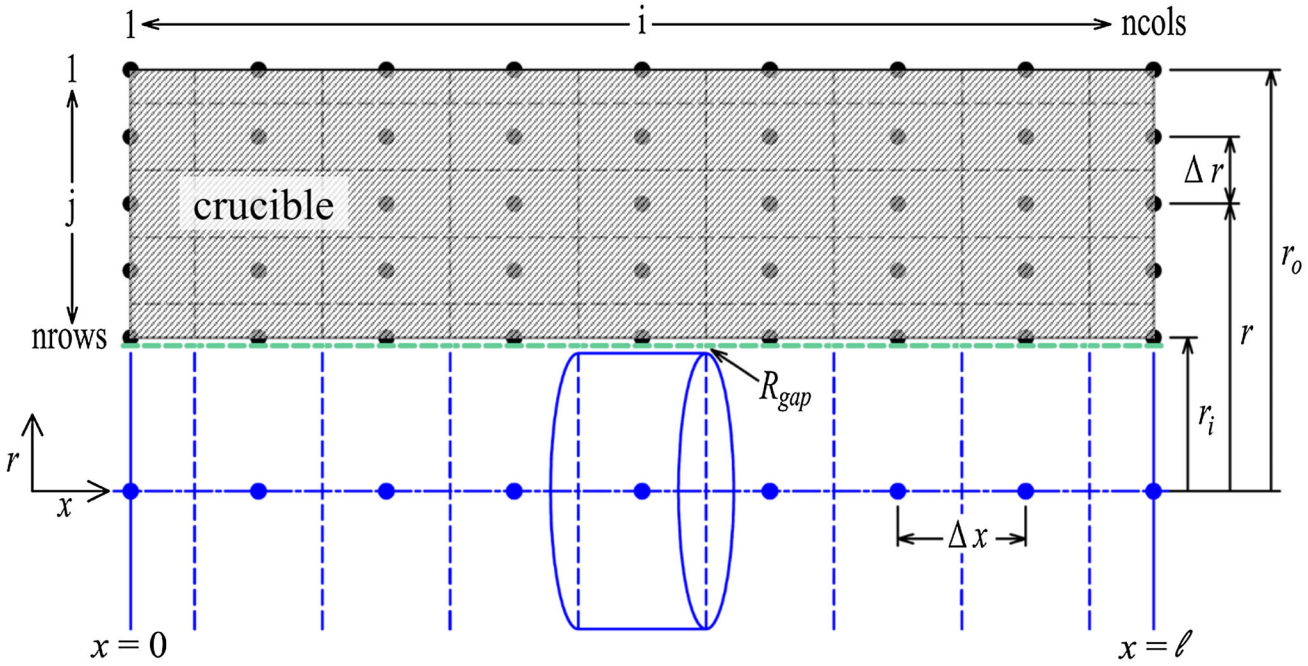

Fig. 4. Axisymmetric model domain of the sample and crucible.

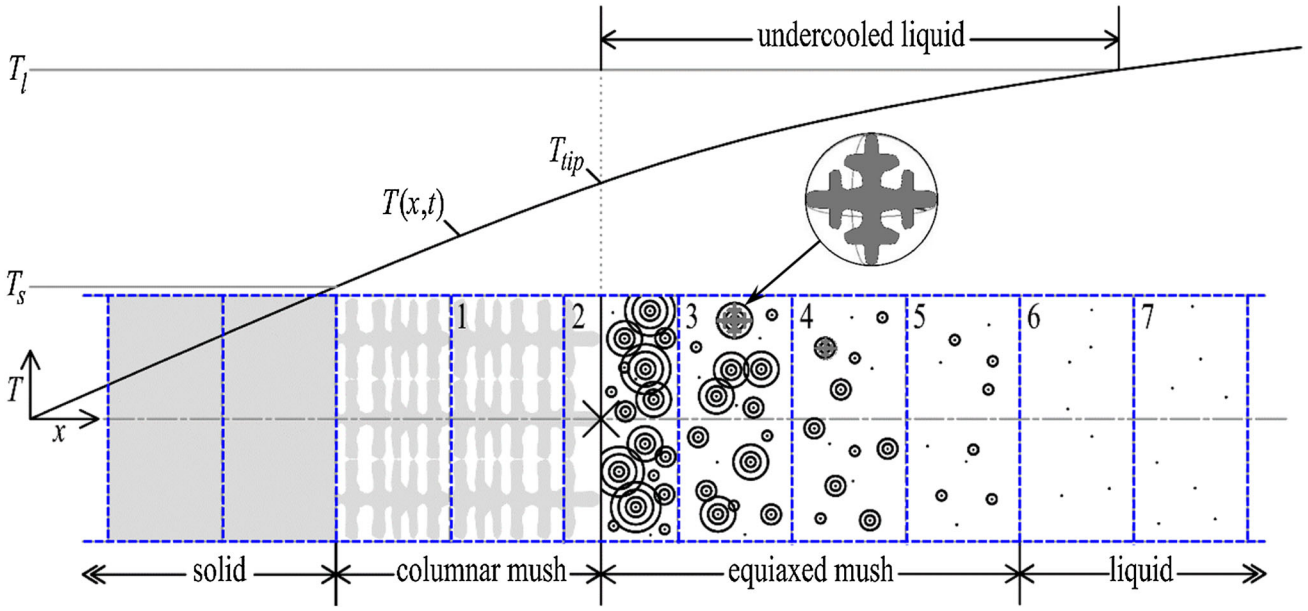

Fig. 5. Spherical equiaxed envelopes growing in undercooled liquid and positive temperature gradient ahead of a columnar front (×) in the BFFTM domain.

cells is superimposed on to the FE mesh and used by the CA method. Each cell is precisely located in one FE element, and the macroscopic fields may be interpolated at the cell scale if required.

The results of 2D CAFE modeling of the grain structure evolution and the occurrence of the CET for some CETSOL Batch1 experiments are already published.[2,20,21] Qualitative agreement was obtained for the position of CET and the CET transition mode, which is sharp in B1-FM1 and progressive in B1-FM5. More comparisons of the distributions of grain elongation factor and equivalent diameter were conducted and revealed a fair quantitative agreement.

Now, the CAFE model was extended to the simulation of the B1-FM1 experiment in three-dimensional (3D). Simulation is restricted to the material without considering the whole equipment and its effect on temperature evolution. The sample is virtually divided, and simulation of the

solidification process is limited to the single domain of interest corresponding to positions from thermocouple TC5 to TC12. Initially, the whole simulation domain is made of a homogeneous liquid of nominal concentration. A Dirichlet boundary condition is used to impose the temperature at the position of the thermocouples. At the macroscopic scale, the energy and solute mass conservations are solved assuming constant densities and fixed solids. Simulation is based on the FE method with about 42,000 isotropic and homogeneous elements and about 9000 nodes using linear interpolation. At the microscopic scale, the Wang-Beckerman model of microsegregation is used with primary arm spacing λ_1 = 1000 μm and secondary arm spacing λ_2 = 78 μm.[20] These values are the mean experimental values determined from sample B1-FM[13] and sample B1-FM[1,2] having the same process parameters. Nucleation occurs at the bottom of the simulated part of the sample (TC5). Growth kinetics is approximated with the Ivantsov solution and the marginal stability criterion using $\sigma = (4\pi^2)^{-1}$. The CA simulation is developed with 3 million cells with a characteristic size of 80 μm. The time step is taken equal to 1 s. The parallelized computation took approximately 90 min on 40 CPUs. The results of the simulation can be seen on Fig. 6 for various solidification times.

As a result of the local temperature history and the nucleation parameters, only a columnar grain structure can first develop, the dendrite growth undercooling being too small to favor nucleation of equiaxed grains. After 2000s (see Table I), velocity is increased and so is the columnar front undercooling. Liquid cells exist ahead of the columnar front containing a nucleation site sufficiently undercooled to give birth to equiaxed grains. As can be seen by comparison of the simulation and experimental grain structure, qualitative comparison is reached. Moreover, the CET position is accurately and precisely predicted. The CET is measured at 133.2 mm using the same criterion as in Ref. 3 with

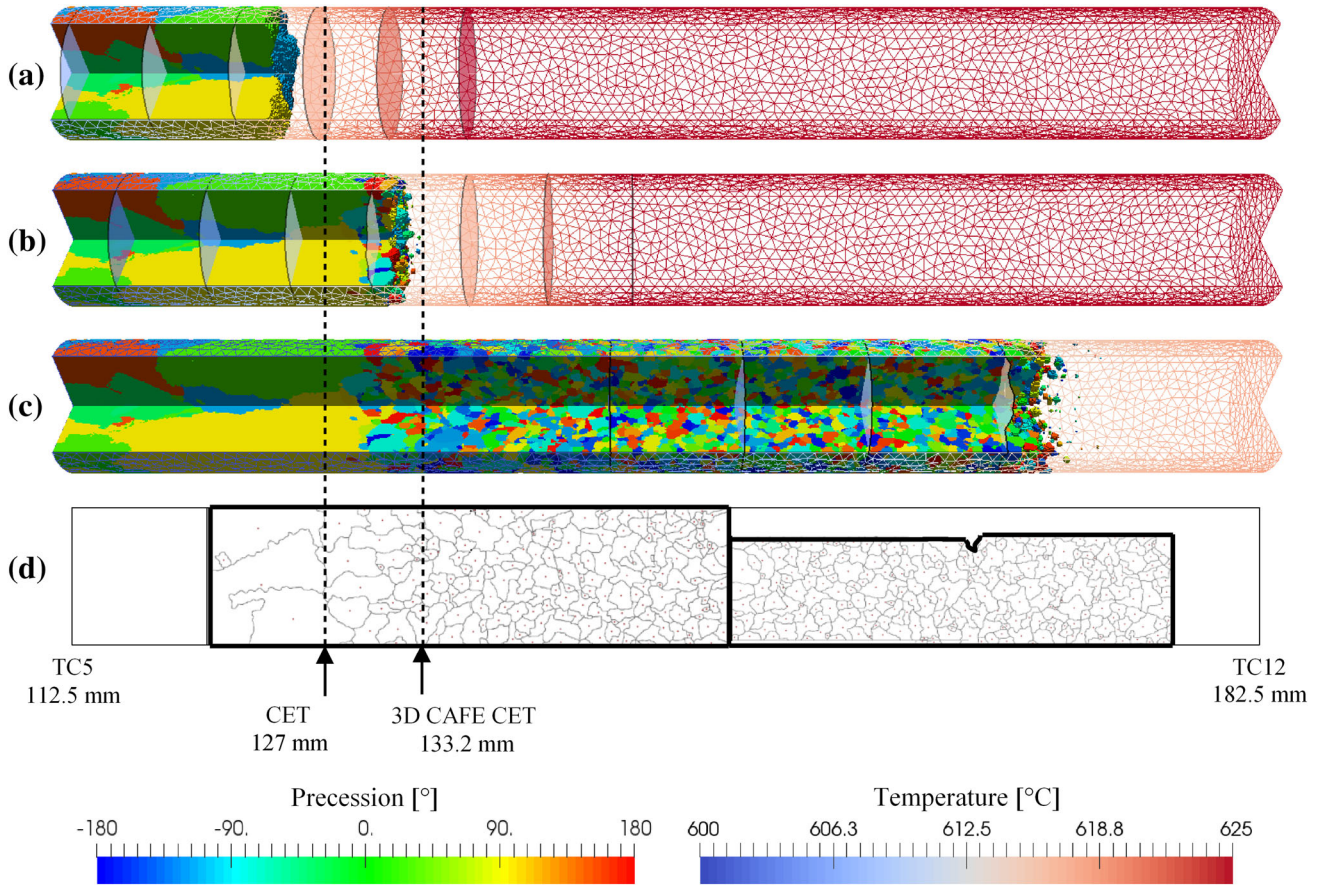

Fig. 6. CAFE simulation of the solidification grain structure of the B1-FM1 sample between thermocouples TC5 (112.5 mm) and TC12 (182.5 mm). Isothermal surfaces from 602°C to 626°C with a step of 4°C are shown. A quarter of the cylinder was removed by postprocessing to offer an exploded view at various times of (a) columnar growth at t = 1800 s, (b) nucleation and growth of equiaxed grains triggered by a sudden increase of the withdrawal rate at t = 2140 s, and (c) the equiaxed structure forming at t = 2400 s. The position of the CET favorably compares with the (d) experimental grain structure observed in a longitudinal metallographic cross section.[3]

3D data inducing a larger error (Fig. 6). The relative error with the experiments is less than 5%. Previous exhaustive explanations[20,21] of the CET appearance remain valid. The velocity jump increases the constitutional undercooling leading to heterogeneous nucleation of equiaxed grains blocking the columnar front.

To improve the present computations further, the methodology developed within the DNN model (see next section) for computation of the dendrite tip growth kinetics is currently under implementation in the CAFE model.

CET Modeling Using DNN Method

To model the CET in microgravity experiments, we use a 3D multiscale DNN method that tracks the diffusion-controlled dynamics of branches of the hierarchically structured dendritic network to model the solidification of dendritic alloys on the grain scale. This approach models explicitly the growth kinetics of all branches of the hierarchical dendritic network (including primary, secondary, and tertiary branches) interacting via the solutal field under both nonsteady-state and steady-state growth conditions. The DNN model describes the dendritic tip as a paraboloid,[22,23] and the dynamic of each dendrite is prescribed by two conditions that determine the evolution of its tip velocity V and radius ρ.[24]

We model the two CETSOL experiments B1-FM1 and B1-FM5 (see Table I). To investigate the CET, the DNN model is discretized in space on a finite-difference cubic grid, and the code is implemented on graphical processing units (GPUs) using the compute unified device architecture (CUDA). To keep the simulations computationally tractable, we study the CET in a 3D rectangular slab geometry of dimensions $L_x \times L_y \times L_z$ with $L_y = 7$ mm (~experimental sample diameter), L_x chosen large enough to include the CET, and the slab thickness $L_z = 1$ mm chosen much smaller than L_y or L_z but large enough to model 3D dendrite growth kinetics accurately.

The tip selection parameter $\sigma = 0.058$ is used in this study.[23,24] We model the growth of randomly oriented grains ahead of the columnar front by incorporating nucleation on foreign inoculant particles randomly located in the melt. We choose a nucleation undercooling $\Delta T_n = 4$ K[2] and an effective density 1.25/mm^3 [1]; the values are determined from the experiments. We use the measured temperatures at the 12 thermocouples along the sample as input data into the model. The initial condition consists of an array of columnar dendrites[23] with an undercooling ΔT_c^{ini} that was varied in the range of 2–8 K; the results are independent of the choice of initial undercooling within this range.

The results of the DNN simulations for samples B1-FM1 and B1-FM5 are shown in Fig. 7. Figure 7a and b shows the grain structures for the FM1 (a) and FM5 (b) samples. Figure 7c and d shows the corresponding temperature–time curves collected from the 12 thermocouples (thin, black dashed lines) and the temperature of the most advanced columnar front T_c (solid red lines) in FM1 (c) and FM5 (d) samples. We measured the starting CET position (CET_{min}) and the ending CET position (CET_{max}) in simulations, where CET_{min} is defined as the position along the sample where the first nucleant particle is initiated, and CET_{max} is defined as the final position of the tip of the most advanced surviving columnar dendrite. In the CETSOL experiments,[1–3] a sharp CET is observed in FM1 (CET_{min} = 125 mm and CET_{max} = 129 mm) and a more progressive CET is observed in FM5 (CET_{min} = 130 mm and CET_{max} = 156 mm). In reasonably good quantitative agreement with those measurements, the simulated grain structures predict that the CET is sharp in FM1 (Fig. 7a with CET_{min} = 129 mm and CET_{max} = 133 mm) and more progressive in FM5 (Fig. 7b with CET_{min} = 146 mm and CET_{max} = 160 mm). In the insets of Fig. 7c and d, we show zoomed-in views of

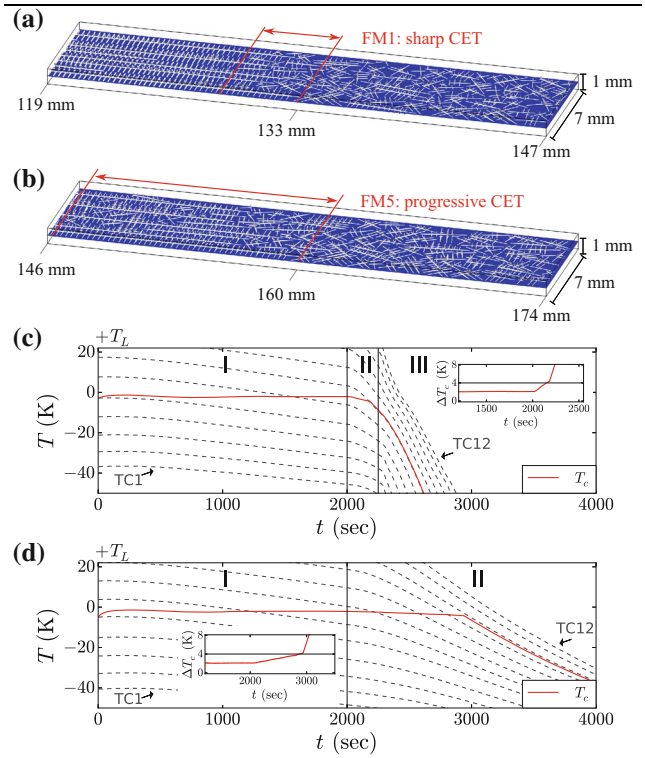

Fig. 7. DNN simulations of dendritic network and grain structures for Al-7 wt.% Si samples for B1-FM1 (a) and B1-FM5 (b) samples (see Table I). A sharp CET is observed in FM1 (CET_{min} = 125 mm and CET_{max} = 129 mm), and a more progressive CET is observed in FM5 (CET_{min} = 130 mm and CET_{max} = 156 mm).[2] (c) and (d) show the temperature curves recorded from 12 thermocouples (thin black dashed lines labelled TC1 to TC12) and the temperature of the most advanced columnar front T_c (solid red lines) in FM1 (c) and FM5 (d). The insets of (c) and (d) show zoomed-in views of the time evolution of the columnar front undercooling ΔT_c. The solid line represents the nucleation undercooling ΔT_n = 4 K, which is used in simulations.

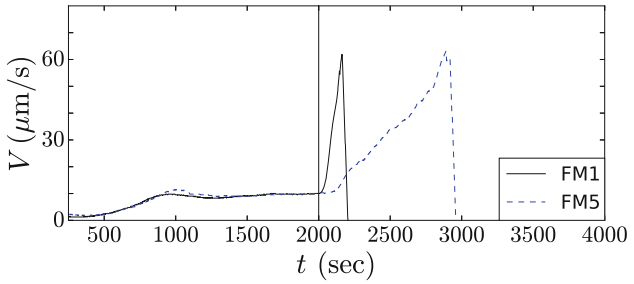

Fig. 8. Time evolution of the velocity of the most advanced columnar front for Batch1 FM1 and FM5 in DNN simulations. The front velocity increases during the growth competition of columnar dendrites leading to an increase of primary spacing ($t <$ 1000 s). After this transient regime, the columnar front grows at a constant velocity. The front velocity increases again upon faster cooling during stage II and drops abruptly when columnar growth is blocked by the nucleated equiaxed grains.

the front undercooling ΔT_c versus time profiles (solid red lines) compared with the nucleation undercooling $\Delta T_n = 4$ K (horizontal solid black lines) in FM1 and FM5 samples, respectively. Only when $\Delta T_c > \Delta T_n$ ($t >$ 2150 s in FM1 and $t >$ 2900 s in FM5), nucleation can take place ahead of the columnar front, thereby allowing equiaxed grains to develop and block columnar growth.

Figure 8 further shows the time evolution of the velocity of the most advanced columnar front in simulations. The growth velocity increases initially during a transient growth regime occurring early in stage I ($t <$ 1000 s), which is associated with a coarsening of the primary spacing. After this transient growth regime, the columnar front reaches a steady-state growth regime with a constant velocity for the rest of stage I. Upon faster cooling during stage II, the front velocity increases again leading to a transient growth regime with a nonuniformity of the primary spacing before the onset of the CET as clearly seen in Fig. 7a. Two types of CET are observed in simulations as mentioned (a sharp CET in FM1 and a progressive CET in FM5). We attribute this difference to the different cooling processes applied at stage II (t = 2000–2250 s in FM1 and t = 2000–4000 s in FM5). For all times after the start of stage II, the front undercooling ΔT_c is always larger in FM1 than in FM5 because of the faster movement of the furnace during this stage, which boosts the nucleation ahead of the columnar front and results in a sharper CET.

Summarizing, DNN modeling predictions for the positions and spatial extent of the CET are in reasonably good quantitative agreement with experimental measurements in two Batch1 samples (B1-FM1 and B1-FM5) that exhibit sharp or progressive CET depending on the thermal conditions. As a next step in this project, DNN simulations will be extended to cylindrical bulk samples. This will allow us to compare simulated 3D grain structures to measurements of grain size and orientation using serial sectioning.[25] Furthermore, the DNN method will be used to model the growth of equiaxed dendrites solidified in microgravity in the transparent model alloy Neopentylglycol-(d)Camphor during the sounding rocket mission MASER-13.

CONCLUSION

This article summarizes the results obtained so far from solidification experiments on-board the ISS by the CETSOL team. In the Materials Science Laboratory, Al-7 wt.% Si alloys with and without grain refiners were solidified in diffusive conditions. Detailed analysis of the microstructure and the grain structure showed columnar growth with some fragments in the case of nonrefined alloy. CET was detected only for refined alloys. In the case of the sudden increase of the solidification velocity, a sharp CET within a few millimeter distance was observed. A progressive CET mode exists in the case of a continuous decrease of the temperature gradient. This mode is characterized by a longer transition region with elongated equiaxed grains followed by fully equiaxed growth.

The unique experimental data basis was used for numerical modeling of CET with three different methods:

1. A front tracking model using an equiaxed growth model that applies JMAK theory; predicts the columnar dendrite tip undercooling, growth rate, and temperature gradient with respect time; and sharp or progressive CET. Good agreement is found between the simulated and the experimentally measured CET position (B1-FM2).
2. Using a CAFE model, both segregation and grain structures, as well as CET, were numerically modeled in 3D. The CET transition mode, be it sharp or progressive, is retrieved. Distributions of grain elongation factor and equivalent diameter are fairly reproduced. Moreover, the CET positions are predicted accurately and precisely.
3. To predict CET, a 3D multiscale DNN method was used. The model was applied to two Batch1 flight samples with sharp and progressive CET (B1-FM1 and B1-FM5), using a simplified slab-like geometry. The DNN modeling predictions for the positions and spatial extent of the CET are in reasonably good quantitative agreement with experimental measurements in both cases.

OUTLOOK

The experimental data basis for description of CET under diffusive conditions will be extended in the coming years. Therefore, within the CETSOL project, solidification experiments with three

different hypoeutectic AlCu alloys, with and without grain refiner, will be performed in reduced gravity on the ISS. Applying different cooling conditions may result in different types of CET. Selected parts of these samples and of the already processed Al-7 wt.% Si samples will additionally be used for a 3D reconstruction of the grain structure by serial sectioning.[25,26] Such 3D features of the structures will be investigated to improve the knowledge of the grain competition, microstructure formation, and CET. In addition, these results will be coupled with further numerical simulations, especially in 3D.

To investigate the dynamics of columnar and equiaxed growth as well as of the CET, further use will be made of the transparent organic alloy Neopentylglycol-(d)Camphor system that solidifies like a metal. As part of the CETSOL project, the sounding rocket experiment MEDI (multiple equiaxed dendrite interaction) was performed on the MASER-13 sounding rocket flight to observe in situ free dendrite growth and solutal interaction between close crystals in this alloy under microgravity conditions without sedimentation of the equiaxed crystals and melt flow.[27] This experiment has already provided valuable benchmark data for modeling equiaxed growth at different length scales. This transparent alloy system will be used for future experiments in the Materials Science Glovebox onboard the ISS. Therefore, on behalf of ESA, the TRANSPARENT facility is under development.[28] Experiments with different (d)Camphor compositions, especially the time-dependent evolution of CET for different cooling conditions, will be investigated using optical charge-coupled device (CCD) cameras. Again, the results will be used to improve modeling of dendrite growth and interaction.

ACKNOWLEDGEMENTS

This work has been carried out as part of the CETSOL European Space Agency microgravity application program (ESTEC Contract Number 14313/01/NL/SH). The authors would like to acknowledge funding by the German BMWi/DLR (FKZ 50WM1443), and the financial support of the Enterprise Ireland via European Space Agency PRODEX Programme (Contract Number 4000107132). A. Karma and C.-H. Chen acknowledge support of NASA Grant NNX14AB34G. The authors acknowledge Hydro-Aluminium Rolled Products GmbH for providing the alloys for the flight samples.

REFERENCES

1. G. Zimmermann, L. Sturz, B. Billia, N. Mangelinck-Noël, H. Nguyen Thi, C.-A. Gandin, D.J. Browne, and W.U. Mirihanage, *JOP Conference Series* 327 (2011).
2. G. Zimmermann, L. Sturz, B. Billia, N. Mangelinck-Noël, D.R. Liu, H. Nguyen Thi, N. Bergeon, C.-A .Gandin, D.J. Browne, Ch Beckermann, D. Tourret, and A. Karma, *Mater. Sci. Forum* 790, 12 (2014).
3. D.R. Liu, N. Mangelinck-Noël, C.A. Gandin, G. Zimmermann, L. Sturz, H. Nguyen Thi, and B. Billia, *Acta Mater.* 64, 253 (2014).
4. W.U. Mirihanage, D.J. Browne, G. Zimmermann, and L. Sturz, *Acta Mater.* 60, 6362 (2012).
5. Y.Z. Li, N. Mangelinck-Noël, H. Nguyen-Thi, G. Zimmermann, L. Sturz, T. Cool, E.B. Gulsoy, and P.W. Voorhees, in *Proceedings of the 6th Decennial International Conference on Solidification SP17*, in press (2017).
6. C.A. Gandin, *Acta Mater.* 48, 2483 (2000).
7. J.D. Hunt, *Mater. Sci. Eng.* 65, 75 (1984).
8. D.J. Browne and J.D. Hunt, *Numer. Heat Trans. B* 45, 395 (2004).
9. W.U. Mirihanage and D.J. Browne, *Comput. Mater. Sci.* 46, 777 (2009).
10. W.U. Mirihanage, D.J. Browne, L. Sturz, and G. Zimmermann, *IOP Conf. Ser. Mater. Sci. Eng.* 27 (2011).
11. R.P. Mooney, S. McFadden, M. Rebow, and D.J. Browne, *Trans. Indian Inst. Met.* 65, 527 (2012).
12. R.P. Mooney, S. McFadden, Z. Gabalcová, and J. Lapin, *Appl. Therm. Eng.* 67, 61 (2014).
13. W.A. Johnson and R.F. Mehl, *Trans. Aime* 135, 396 (1939).
14. M. Avrami, *J. Chem. Phys.* 9, 177 (1941).
15. A.N. Kolmogorov, *Bull. Acad. Sci. URSS (Sci. Math. Nat.)* 3, 355 (1937).
16. T. Carozzani, H. Digonnet, and C.-A. Gandin, *Model. Simul. Mater. Sci. Eng.* 20, 015010 (2012).
17. T. Carozzani, Ch.-A. Gandin, H. Digonnet, M. Bellet, K. Zaidat, and Y. Fautrelle, *Metall. Mater. Trans. A* 44, 873 (2013).
18. T. Carozzani, Ch.-A. Gandin, and H. Digonnet, *Model. Simul. Mater. Sci. Eng.* 22, 015012 (2014).
19. Ch.-A. Gandin, T. Carozzani, H. Digonnet, S. Chen, and G. Guillemot, *JOM* 65, 1122 (2013).
20. D.R. Liu, N. Mangelinck-Noël, Ch.-A. Gandin, G. Zimmermann, L. Sturz, H. Nguyen-Thi, and B. Billia, *Acta Mater.* 93, 24 (2015).
21. D.R. Liu, N. Mangelinck-Noël, Ch.-A. Gandin, G. Zimmermann, L. Sturz, H. Nguyen-Thi, B. Billia, and I.O.P. Series, *Mater. Sci. Eng.* 117, 012009 (2016).
22. D. Tourret, A. Karma, A.J. Clarke, P.J. Gibbs, and S.D. Imhoff, *IOP Conf. Ser. Mater. Sci. Eng.* 84, 012082 (2015).
23. D. Tourret and A. Karma, *Acta Mater.* 120, 240 (2016).
24. D. Tourret, A.J. Clarke, S.D. Imhoff, P.J. Gibbs, J.W. Gibbs, and A. Karma, *JOM* 67, 1776 (2015).
25. J.L. Fife and P.W. Voorhees, *Acta Mater.* 57, 2418 (2009).
26. J. Alkemper and P.W. Voorhees, *Acta Mater.* 49, 897 (2001).
27. L. Sturz, M. Hamacher, and G. Zimmermann, in *Proceedings of the 6th Decennial International Conference on Solidification SP17*, in press (2017).
28. A. Ludwig, J. Mogerisch, M. Kolbe, G. Zimmermann, L. Sturz, N. Bergeon, B. Billia, G. Faivre, S. Akamatsu, S. Bottin-Rousseau, and D. Voss, *JOM* 64, 1097 (2012).